Low-Q whispering gallery modes in anisotropic metamaterial shells

Ana Díaz-Rubio, Jorge Carbonell, Daniel Torrent, and José Sánchez-Dehesa*

Wave Phenomena Group, Department of Electronics Engineering, Universitat Politècnica de València, Camino de Vera, s.n. (Building 7F), ES-46022 Valencia, Spain

(Received 10 May 2013; revised manuscript received 31 July 2013; published 10 September 2013)

Anisotropic and inhomogeneous metamaterial shells are studied in order to exploit all their resonant mode richness. These multilayer structures are based on a cylindrical distribution of radially dependent constitutive parameters including an inner void cavity. Shell, cavity, and whispering gallery modes are characterized, and special attention is paid to the latter ones. The whispering gallery modes are created at the boundary layers of the shell with the background. Energy localization is produced with highly radiative characteristics when the localization takes place at the external layer. These low-Q resonant states have frequencies that are independent of the shell thickness. However, their quality factors can be controlled by the number of layers forming the shell, which allows confining electromagnetic waves at the interface layers (internal or external), and make them suitable for the harvesting of electromagnetic energy.

DOI: 10.1103/PhysRevB.88.115118 PACS number(s): 41.20.Jb, 84.40.−x, 84.60.−h

I. INTRODUCTION

Textured surfaces are a means of guiding, absorbing, or reflecting electromagnetic waves. Therefore, the so-called surface or interface modes are a powerful alternative to control the propagation, harvesting, or redirection of electromagnetic waves.[1–3] These phenomena can be selective in frequency or broadband and give rise to a high number of applications in virtually all spectral bands. To mention just a few examples of recent studies, we can cite frequency selective surfaces for microwaves,[4,5] fishnet structures and metasurfaces at terahertz frequencies,[6,7] or surface plasmons in optics.[8,9] One of the key underlying drivers in this topic is the use of building blocks based on geometrical arrangements of unitary constituents at a subwavelength scale. At the same time, this research context has also been boosted by the rise of metamaterials. Metamaterials can be defined as artificial structures based on inclusions or elements with subwavelength dimensions. Using microstructured media allows a description in terms of constitutive parameters, those that govern the behavior of electromagnetic waves. With metamaterials it is possible to tailor constitutive parameters (namely permittivity and permeability) so as to achieve negative, null, or even extreme values for them. These parameters can in turn be related to other effective material magnitudes like the refractive index or the impedance. Although the "material" concept usually entails a bulk dimension, opposed to a two-dimensional system or surface, both areas share a number of common problems and possibilities.

Linked to the discussion above, this work analyzes the presence of interface or whispering gallery modes in anisotropic metamaterial shells. In particular, we focus on cylindrical shells based on radial photonic crystals (RPCs).[10,11] In comparison with the so called circular photonic crystals (CPCs),[12,13] the RPCs are multilayered structures that are invariant under radial translations and verify the Bloch's theorem. This last property is possible in cylindrical coordinates by using anisotropic and radially dependent constitutive parameters, which are feasible using the metamaterial concept.

We are interested here in finite size RPCs, or RPC shells, consisting of a central cavity and a few layers of RPCs. The resonant modes associated with these anisotropic metamaterial shells allow designing devices for different types of applications, like beam shaping shells or position and frequency detectors.[11,14] In addition to the Fabry-Perot-like modes located in the RPC shell, cavity modes exist at the central cavity whose features are equivalent to those predicted for cylindrical cavities,[15] but now the localization is due to the band gap created by the RPC shell. Finally, whispering gallery modes (WGMs) are the third type of resonant modes existing in these structures and they are localized close to the interfaces at the inner and outer boundaries of the RPC shell with the background. This main purpose of this work is the study of these resonances not previously described. As a salient feature, we should cite that WGMs have resonant frequencies that are independent of the shell thickness. We may also point out that there are significant differences with respect to localization when compared to Tamm states, characterized at the surface of dielectric multilayers.[16,17]

The article is organized as follows. After this introduction, Sec. II briefly reviews the main properties of the photonic band structure of RPCs, for the sake of completeness. Then, Sec. III presents a detailed discussion on how the properties of a finite RPC can be obtained using the transfer matrix method (TMM), an analytical model that is able to describe all the resonant features associated with the metamaterial shells under study. Section IV analyzes some characteristics of WGMs in order to consider them as building units of devices for energy harvesting. Finally, Sec. V summarizes the main findings of this work.

II. RADIAL PHOTONIC CRYSTALS: PHOTONIC BAND STRUCTURE

RPCs are a type of crystals (i.e., they accomplish the Bloch theorem) that can be briefly described as periodic structures with anisotropic and radially dependent constitutive parameters.[10] This definition equally applies to their acoustic counterparts, the radial acoustic crystals (RACs), since there is a formal equivalence between both problems.[18] For a critical comparison between RPC and RAC the reader is referred to Refs. 10 and 18.

Here we will focus on electromagnetic waves in cylindrical structures and particularly considering TM^z (E^z polarized) modes. The obtained results can be nevertheless generalized to other arrangements.

Let us consider a RPC in two dimensions (2D) made of alternating layers of type a (thickness d_a) and of type b (thickness d_b) whose constitutive parameters are the following:

$$\mu_{ra}(r) = \frac{\hat{\mu}_{ra}}{r} = \frac{0.25d}{r}, \quad \mu_{rb}(r) = \frac{\hat{\mu}_{rb}}{r} = \frac{0.5d}{r}, \tag{1}$$

$$\mu_{\theta a}(r) = \hat{\mu}_{\theta a} r = \frac{2r}{d}, \quad \mu_{\theta b}(r) = \hat{\mu}_{\theta b} r = \frac{r}{d}, \tag{2}$$

$$\varepsilon_{za}(r) = \frac{\hat{\varepsilon}_{za}}{r} = \frac{d}{1.5r}, \quad \varepsilon_{zb}(r) = \frac{\hat{\varepsilon}_{zb}}{r} = \frac{d}{r}, \tag{3}$$

where r is the radial distance from the center of the cylindrical shell and d is the period of the multilayered structure ($d = d_a + d_b$). From these values the components of the refractive index tensor are calculated as follows: the radial component is $n_r = \sqrt{\mu_\theta \varepsilon_z}$, while the angular component is $n_\theta = \sqrt{\mu_r \varepsilon_z}$. Figure 1(a) schematically shows a truncated RPC made of five periods, and Figs. 1(b)–1(c) depict the profiles of the parameters described by Eqs. (1) to (3).

It has been proven[10] that the photonic band structure can be calculated as

$$\cos(Kd) = \cos(k_{aq}d_a)\cos(k_{bq}d_b) - \frac{1}{2}\left(\frac{\hat{\mu}_{\theta b}}{\hat{\mu}_{\theta a}}\frac{k_{aq}}{k_{bq}} + \frac{\hat{\mu}_{\theta a}}{\hat{\mu}_{\theta b}}\frac{k_{bq}}{k_{aq}}\right)\sin(k_{aq}d_a)\sin(k_{bq}d_b), \tag{4}$$

where K represents the Bloch wave number corresponding to the multilayered structure and k_a and k_b represent the k vectors in layers a and b, respectively.

The solution for this equation using the parameters described in Eqs. (1)–(3) is displayed in Fig. 2(a), where q denotes the symmetry order of the modes in the corresponding band. Note that each band contains modes with well-defined symmetry. In addition, note that modes with coefficient $q > 0$ have a cutoff frequency higher than zero. Also, part of the $q = 1$ band (with dipolar symmetry modes) is inserted within the first band gap of mode $q = 0$ (with monopolar modes).

Let us stress that by changing the material parameters in Eqs. (1)–(3) it is possible to perform a band gap engineering and design photonic structures that fit our needs. For example, in Fig. 2(a) we observe that part of the first band of the modes with dipolar symmetry is in the band gap of the rest of the modes. This implies that only dipolar modes will be excited by external sources in the frequency region [0.38–0.55] (in reduced units). This feature can be extremely useful for designing photonic devices based on finite size RPCs. The modeling of these interesting structures is described below.

III. METAMATERIAL SHELLS BASED ON 2D RPCS: ANALYTICAL MODEL

Let us consider now the case of a finite RPC consisting of N periods and a void central cavity of radius r_{int}. Figure 1(a) shows a scheme of a finite size RPC consisting of a five period multilayer with an inner air cavity of radius equivalent to the thickness of two periods ($r_{\text{int}} = 2d$). The resulting anisotropic

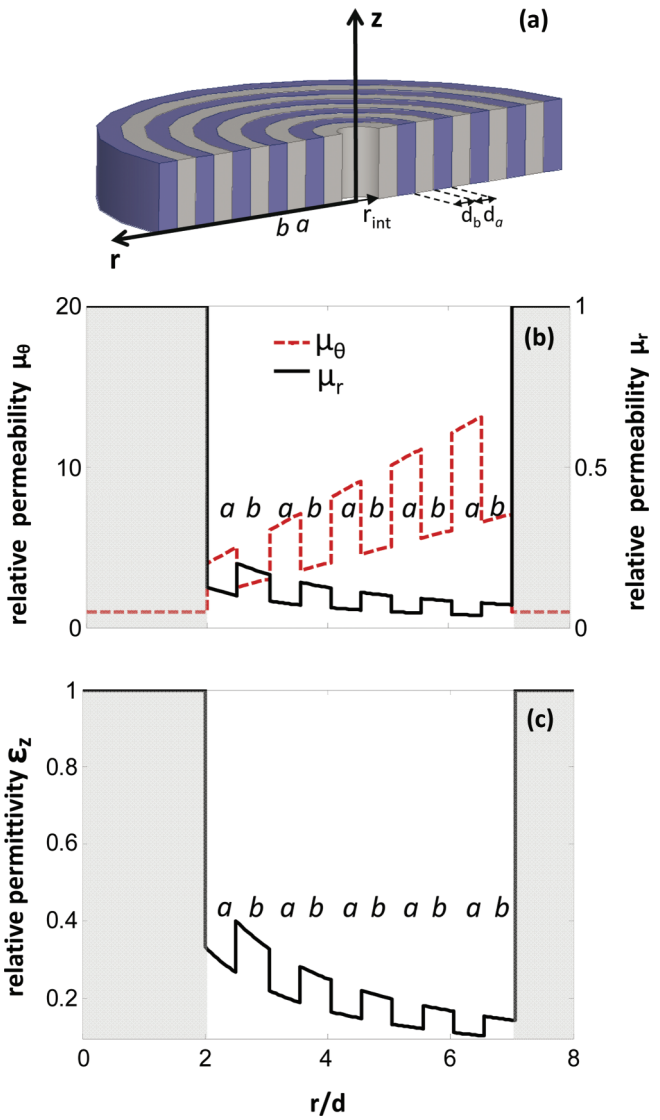

FIG. 1. (Color online) (a) Schematic picture of a truncated radial photonic crystal. The resulting metamaterial shell has an inner void cavity of radius $r_{\text{int}} = 2d$ and five periods of alternating type-a and type-b materials. (b) Profiles of the radial (μ_r) and angular (μ_θ) permeabilities as a function of the radial distance. (c) Profile of the dielectric permittivity ε_z.

and inhomogeneous metamaterial shells are studied here by means of the transfer matrix method[19] (TMM), which is a suitable procedure for describing their rich resonant behavior.

The TM^z polarized field at an arbitrary point (r, θ) in the 2D space can be expressed in cylindrical coordinates as

$$E_z(r,\theta) = \sum_q E_q(r)\, e^{iq\theta}. \tag{5}$$

In homogeneous and isotropic media, electric fields can be represented by a linear combination of Bessel and Hankel functions:

$$E_q(r,\theta) = [C_{iq}^{+} H_q(k_i r) + C_{iq}^{-} J_q(k_i r)]e^{iq\theta}, \tag{6}$$

where $k_i^2 = \omega^2 \varepsilon_i \mu_i$ with $i = 1,2$. Materials 1 and 2 are the materials inside the inner cavity and in the external

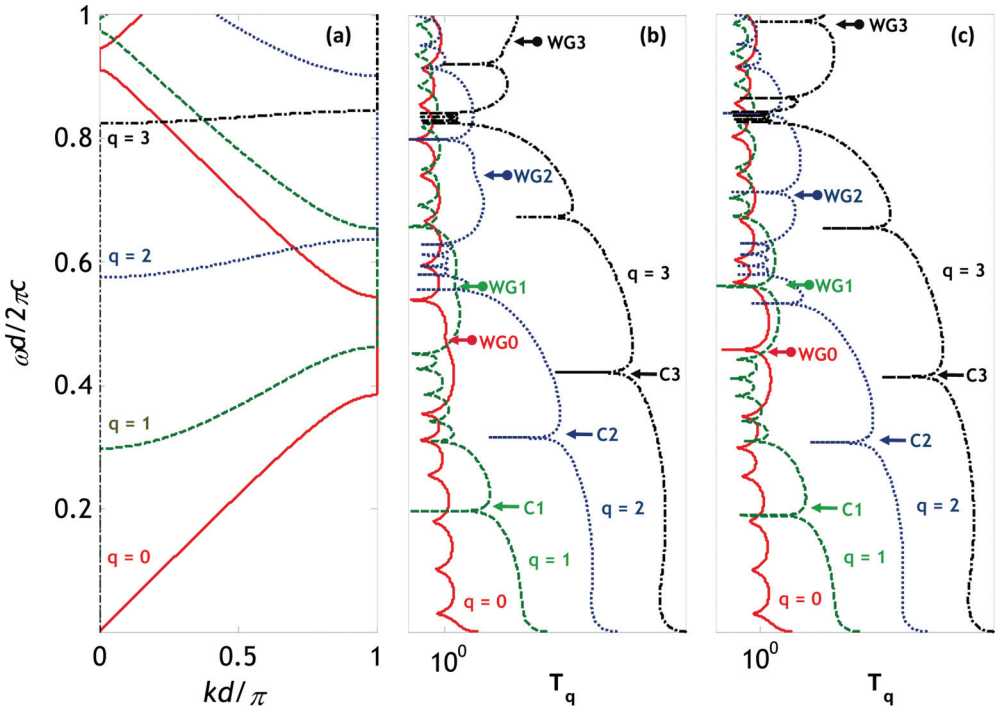

FIG. 2. (Color online) (a) Photonic band structure for the radial photonic crystal described in Sec. II. (b) Calculated transmission coefficients T_q for the five period metamaterial shell described in Fig. 1. (c) Calculated transmission coefficients T_q for a structure similar to Fig. 1 but with inverted a and b layer order ($abab\ldots$ changes to $baba\ldots$). The peaks in a given T_q curve represent resonant modes with q symmetry. The cavity (C) and whispering gallery (WG) modes are marked with arrows. The unmarked peaks correspond to Fabry-Perot (FP) modes and are mostly located within the shell.

background, respectively. Note that this expression allows us to obtain the field produced by external sources located at any position inside the cavity ($r < r_{\rm int}$).

In turn, electric fields inside the RPC shell ($r > r_{\rm int}$) can be cast as[10,11,14]

$$E_q(r,\theta) = [(C_q^+)_{ln} e^{ik_{lq}(r'-nd)} + (C_q^-)_{ln} e^{-ik_{lq}(r'-nd)}] e^{iq\theta}, \quad (7)$$

where

$$k_{lq}^2 = \hat{\varepsilon}_{zl}\hat{\mu}_{\theta l}\omega^2 - q^2\frac{\hat{\mu}_{\theta l}}{\hat{\mu}_{rl}}, \quad (8)$$

$r' = r - R_a$, $n = 1,2,\ldots,N$, and $l = a,b$.

The electric fields in two consecutive layers are related through the corresponding boundary conditions. Thus, for the E^z polarized modes under study:

$$E_z(r,\theta)|_{r=r_{\rm int}^+} = E_z(r,\theta)|_{r=r_{\rm int}^-}, \quad (9)$$

$$\frac{1}{\mu(r)}\frac{\partial E_z(r,\theta)}{\partial r}\bigg|_{r=r_{\rm int}^+} = \frac{1}{\mu(r)}\frac{\partial E_z(r,\theta)}{\partial r}\bigg|_{r=r_{\rm int}^-}. \quad (10)$$

These conditions are imposed at the interfaces of the unit cell. Therefore, the matrix relating the complex amplitudes of the plane waves in a b layer with those of the equivalent layer of the next unit cell is

$$\begin{pmatrix}(C_q^+)_{bn-1}\\(C_q^-)_{bn-1}\end{pmatrix} = \begin{pmatrix}A & B\\C & D\end{pmatrix}\begin{pmatrix}(C_q^+)_{bn}\\(C_q^-)_{bn}\end{pmatrix}, \quad (11)$$

where the transmission matrix $ABCD$ elements are

$$A = e^{-ik_{bq}d_b}\left[\cos(k_{aq}d_a) - \frac{1}{2}i\left(\frac{\hat{\mu}_{\theta b}}{\hat{\mu}_{\theta a}}\frac{k_{aq}}{k_{bq}} + \frac{\hat{\mu}_{\theta a}}{\hat{\mu}_{\theta b}}\frac{k_{bq}}{k_{aq}}\right)\sin(k_{aq}d_a)\right], \quad (12)$$

$$B = e^{ik_{bq}d_b}\left[-\frac{1}{2}i\left(\frac{\hat{\mu}_{\theta b}}{\hat{\mu}_{\theta a}}\frac{k_{aq}}{k_{bq}} - \frac{\hat{\mu}_{\theta a}}{\hat{\mu}_{\theta b}}\frac{k_{bq}}{k_{aq}}\right)\sin(k_{aq}d_a)\right], \quad (13)$$

$$C = e^{-ik_{bq}d_b}\left[\frac{1}{2}i\left(\frac{\hat{\mu}_{\theta b}}{\hat{\mu}_{\theta a}}\frac{k_{aq}}{k_{bq}} - \frac{\hat{\mu}_{\theta a}}{\hat{\mu}_{\theta b}}\frac{k_{bq}}{k_{aq}}\right)\sin(k_{aq}d_a)\right], \quad (14)$$

$$D = e^{ik_{bq}d_b}\left[\cos(k_{aq}d_a) + \frac{1}{2}i\left(\frac{\hat{\mu}_{\theta b}}{\hat{\mu}_{\theta a}}\frac{k_{aq}}{k_{bq}} + \frac{\hat{\mu}_{\theta a}}{\hat{\mu}_{\theta b}}\frac{k_{bq}}{k_{aq}}\right)\sin(k_{aq}d_a)\right]. \quad (15)$$

For the case of a RPC shell made of N unit cells, the following relation applies:

$$\begin{pmatrix} (C_q^+)_{b0} \\ (C_q^-)_{b0} \end{pmatrix} = \begin{pmatrix} A & B \\ C & D \end{pmatrix}^N \begin{pmatrix} (C_q^+)_{bN} \\ (C_q^-)_{bN} \end{pmatrix}. \tag{16}$$

The continuity conditions at the interface between the inner cavity (medium 1) and the RPC shell produce the following transition matrix:

$$\begin{pmatrix} C_{1q}^+ \\ C_{1q}^- \end{pmatrix} = \frac{i\pi\mu_1}{2} \begin{pmatrix} J_q'(k_1R_a) & -J_q(k_1R_a) \\ -H_q'(k_1R_a) & H_q(k_1R_a) \end{pmatrix} \begin{pmatrix} 1 & 1 \\ Z_1 & -Z_1 \end{pmatrix} \begin{pmatrix} (C_q^+)_{b0} \\ (C_q^-)_{b0} \end{pmatrix}, \tag{17}$$

where

$$Z_1 = i\frac{\mu_1 k_{bq}}{k_1 \hat{\mu}_{\theta b} R_a}.$$

The boundary conditions at the interface between the RPC shell and the external background (medium 2) give the second transition matrix:

$$\begin{pmatrix} (C_q^+)_{bN} \\ (C_q^-)_{bN} \end{pmatrix} = \frac{1}{2} \begin{pmatrix} 1 & 1 \\ 1 & -1 \end{pmatrix} \begin{pmatrix} H_q(k_2R_b) & J_q(k_2R_b) \\ Z_2H_q'(k_2R_b) & Z_2J_q'(k_2R_b) \end{pmatrix} \begin{pmatrix} C_{2q}^+ \\ C_{2q}^- \end{pmatrix}, \tag{18}$$

with

$$Z_2 = -i\frac{k_2 \hat{\mu}_{\theta b} R_b}{\mu_2 k_{bq}}.$$

Finally, the complex amplitudes of the E field in the inner cavity and in the external background are related by the overall relation:

$$\begin{pmatrix} C_{1_q}^+ \\ C_{1_q}^- \end{pmatrix} = \begin{pmatrix} M_{11} & M_{12} \\ M_{21} & M_{22} \end{pmatrix} \begin{pmatrix} C_{2_q}^+ \\ C_{2_q}^- \end{pmatrix}, \tag{19}$$

$$M = \frac{i\pi\mu_1}{4\sin(Kd)} \begin{pmatrix} J_q'(k_1R_a) & -J_q(k_1R_a) \\ -H_q'(k_1R_a) & H_q(k_1R_a) \end{pmatrix} \begin{pmatrix} A_N & B_N \\ C_N & D_N \end{pmatrix} \begin{pmatrix} H_q(k_2R_b) & J_q(k_2R_b) \\ Z_2H_q'(k_2R_b) & Z_2J_q'(k_2R_b) \end{pmatrix}. \tag{20}$$

The *ABCD* matrix elements are calculated by a method reported previously[20] and can be written as

$$A_N = \left[2\cos(Kd) + \left(\frac{\hat{\mu}_{\theta b}}{\hat{\mu}_{\theta a}}\frac{k_{aq}}{k_{bq}} - \frac{\hat{\mu}_{\theta a}}{\hat{\mu}_{\theta b}}\frac{k_{bq}}{k_{aq}}\right)\sin(k_{aq}d_a)\sin(k_{bq}d_b)\right]\sin(NKd) - 2\sin[(N-1)Kd], \tag{21}$$

$$B_N = -2i\left[\cos(k_{aq}d_a)\sin(k_{b_q}d_b) + \frac{\hat{\mu}_{\theta a}}{\hat{\mu}_{\theta b}}\frac{k_{bq}}{k_{aq}}\sin(k_{aq}d_a)\cos(k_{bq}d_b)\right]\sin(NKd), \tag{22}$$

$$C_N = -2Z_1 i\left[\cos(k_{aq}d_a)\sin(k_{b_q}d_b) + \frac{\hat{\mu}_{\theta b}}{\hat{\mu}_{\theta a}}\frac{k_{aq}}{k_{bq}}\sin(k_{aq}d_a)\cos(k_{bq}d_b)\right]\sin(NKd), \tag{23}$$

$$D_N = Z_1\left[2\cos(Kd) - \left(\frac{\hat{\mu}_{\theta b}}{\hat{\mu}_{\theta a}}\frac{k_{aq}}{k_{bq}} - \frac{\hat{\mu}_{\theta a}}{\hat{\mu}_{\theta b}}\frac{k_{bq}}{k_{aq}}\right)\sin(k_{aq}d_a)\sin(k_{bq}d_b)\right]\sin(NKd) - 2\sin[(N-1)Kd], \tag{24}$$

where $\cos(Kd)$ is the dispersion diagram described by Eq. (4).

The matrix M in Eq. (20) is used to determine the transmittance (T_q) and the reflectance (R_q) of modes with q symmetry from the RPC shell. Their expressions are

$$T_q = 1/M_{11},\ R_q = M_{21}/M_{11}. \tag{25}$$

Let us recall that these coefficients always refer to the radial propagation direction.

The quality factor (Q) of a given resonant mode can also be obtained from the matrix element $M_{11}(\omega)$ and involves the calculation of the complex frequencies ω_R that cancel this matrix element: $M_{11}(\omega_R) = 0$, where $\omega_R = \omega_0 - i\alpha$. Then, the Q factor can be calculated from the real and imaginary parts of the resonance frequency as $Q = \frac{\omega_0}{2\alpha}$. In the rest of the work, unless otherwise indicated, Q factors are calculated following this procedure.

A. Application of the TMM to a practical case

The TMM has been applied to the finite RPC shell depicted in Fig. 1(a). The profiles of the constitutive parameters are shown in Figs. 1(b) and 1(c). Note that we employ the same constitutive parameters that were employed in the RPC studied in Sec. II for the sake of comparison. The values of the constitutive parameters (in relative units) within the shell always remain positive and roughly vary between 0.1 and 10.

The transmission properties of the shell are depicted in Figs. 2(b) and 2(c). The difference between both cases only comes from the layer ordering. In Fig. 2(b), layer profiles exactly follow the data in Fig. 1, whereas in Fig. 2(c) the order between a and b layers is inverted. Thus, in Fig. 2(b), the inner layer is of a type and outer layer is of b type, but in Fig. 2(c) it is the opposite. The different curves represent the transmittance coefficients T_q for the total transmitted electrical field (E_z^t), whose expression is

$$E_z^t(r,\theta) = \sum_q A_q^0 T_q H_q(k_0 r)\, e^{iq\theta}, \tag{26}$$

where A_q^0 represent the amplitudes of the incident wave modes, T_q give information about the interaction between EM waves and the RPC shell, and H_q are the Hankel functions. Note that a given T_q curve is specifically related to the allowed band with the same q symmetry in the dispersion diagram shown in Fig. 2(a). The peaks observed in a selected T_q spectrum represent the resonant modes with q symmetry in the shell. The different mode types are classified as follows.

1. Fabry-Perot-like modes

If the peaks in the coefficients T_q appear at frequencies contained within the photonic bands of the corresponding dispersion relation [see Fig. 2(a)], they are produced by a Fabry-Perot (FP) interference phenomenon due to the shell finite thickness. Figure 3(a) plots, as an example, the E-field pattern of a FP mode with dipolar symmetry ($q = 1$). Note that the field is mainly located inside the shell, i.e., within the radius range $r_{\text{int}} < r < 5d$. The FP-like resonances have been widely studied in previous works. For a detailed discussion of their properties and their potential application the reader is referred to previous references.[10,11]

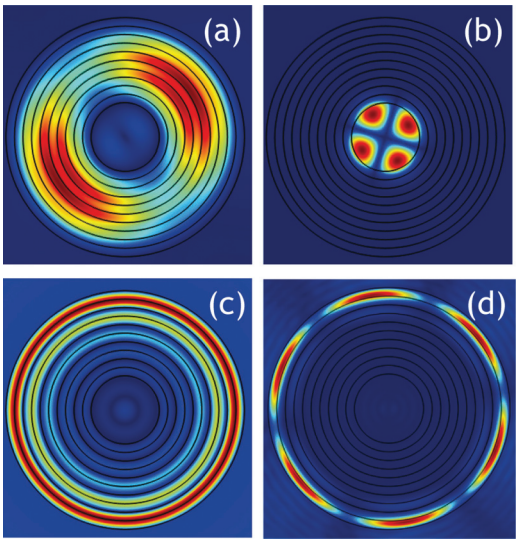

FIG. 3. (Color online) Resonant modes found in the five period RPC shell described in Fig. 1: (a) Fabry-Perot-like mode with symmetry $q = 1$ and frequency 0.3101 (in reduced units), (b) cavity mode with symmetry $q = 2$ and frequency 0.3157 [C2 in Fig. 2(b)], (c) whispering gallery mode with symmetry $q = 0$ and frequency 0.4724 [WG0 in Fig. 2(b)], and (d) whispering gallery mode with symmetry $q = 3$ and frequency 0.9442 [WG3 in Fig. 2(b)].

2. Cavity modes

When the peaks in T_q appear within the band gap of the photonic band with q symmetry, they represent modes that are confined in the central void region. For example, Fig. 2(b) shows that the C1 peak appearing in the profile of the $q = 1$ spectrum (dashed line) corresponds to a cavity mode with dipolar symmetry. C1 has frequency 0.1971 which is below the cutoff of the corresponding band in Fig. 2(a). In a similar manner, peaks C2 and C3 with respective frequencies 0.3157 and 0.4156, are due to the presence of cavity modes with quadrupolar ($q = 2$) and hexapolar symmetry ($q = 3$). Note how the positions of these low frequency modes are the same for the configuration studied in Fig. 2(c); the reason for this is the lack of interaction with the WGMs, which appears at higher frequencies.

Figure 3(b) displays as an example the E-field pattern corresponding to the cavity mode with quadrupolar symmetry ($q = 2$). Let us stress that cavity modes are strictly related to the size of the inner cavity and, as it is shown in Fig. 3(b), they are strongly localized inside the cavity. Their properties will be further discussed in Sec. IV.

3. Whispering gallery modes

In addition to the resonant modes previously described, we have observed additional features in the transmission spectra that have been associated with WGMs. The shoulders annotated in Fig. 2(b) as WG0, WG1, WG2, and WG3 are produced by resonant modes characterized by having their E field mainly localized in the last (external) layer of the shell, as it is usual for WGMs described in the literature. In the case of Fig. 2(c) the same WGM are localized in the most inner layer of the shell at slightly shifted frequencies and with sharper transmittance peaks. The frequencies of modes WG0, WG1, WG2, and WG3 have been obtained independently using a method based on finite elements[21] and their values are 0.4724, 0.5607, 0.7667, and 0.9442 (in reduced units). These values are in agreement with the frequencies at which the shoulders appear in the corresponding T_q curves (with $q = 0$ to 3).

The WGMs are characterized by two main properties. On the one hand, their frequencies are always within the band gap of the photonic bands with the same symmetry. On the other hand, they appear in a truncated RPC with a void cavity at its center. In other words, the structures sustaining WGMs are anisotropic shells having two boundaries with the background. For the case under study here, the external and inner borders are at $r_{\text{ext}} = 7d$ and $r_{\text{int}} = 2d$, respectively.

Figures 3(c) and 3(d) display, as two typical examples, the E-field patterns of WGMs with symmetries $q = 0$ and $q = 3$, respectively; WG0 and WG3 in Fig. 2(b). It is shown that E fields are mainly localized at the shell outer layers.

Figure 4(a) specifically shows the E-field profile, along the diameter crossing the horizontal axis, for the mode WG0 with frequency 0.4724. A comparison with the profiles of the components of the refractive index tensor, which are shown in

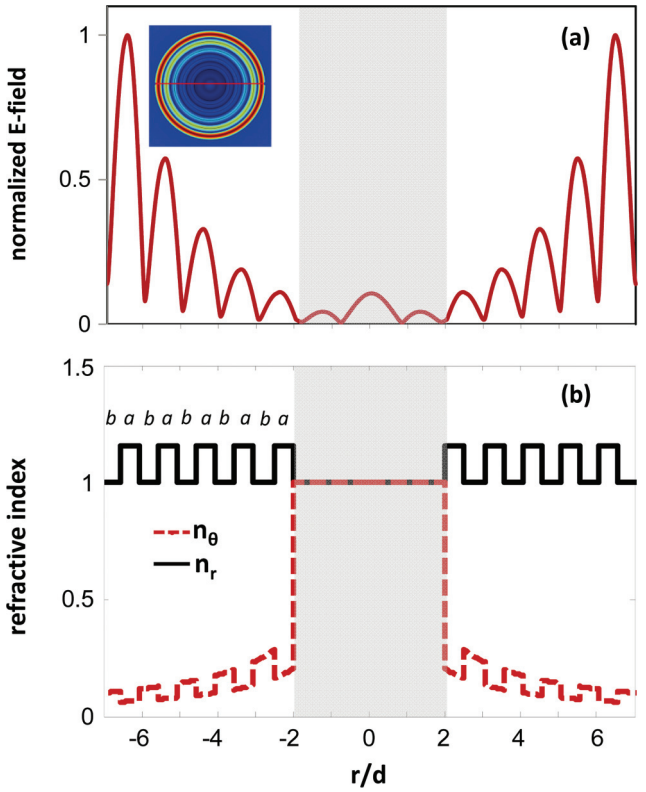

FIG. 4. (Color online) (a) The E-field profile along a diameter section of a WG mode located at the outer layer of the five period RPC shell described in Fig. 1. The monopolar mode WG0 with frequency 0.4724 is depicted. Note how the field amplitude exponentially decreases with the separation from the external boundary. The inset shows the E-field pattern in 2D for comparison purposes. (b) Radial dependence of the radial and angular components of the refractive index tensor.

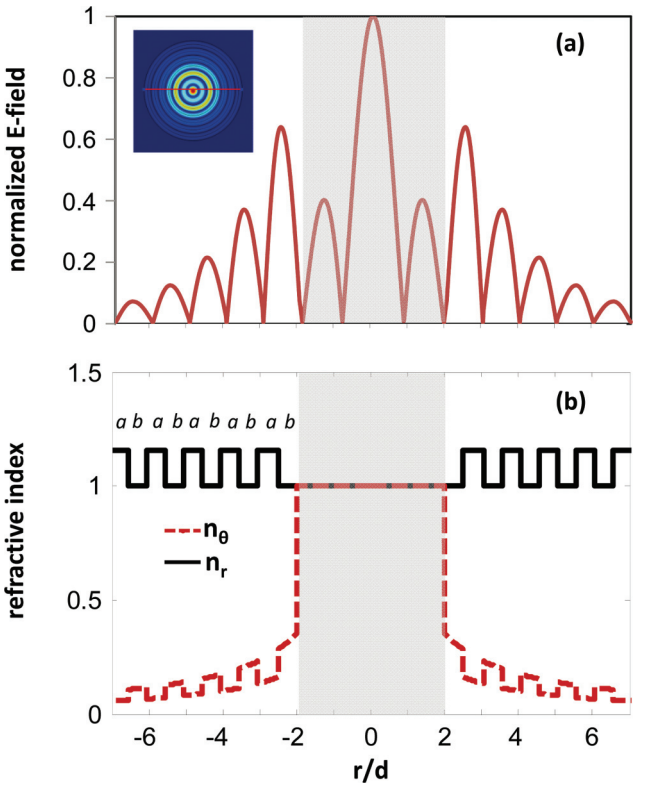

FIG. 5. (Color online) (a) The E-field profile along a diameter section of a WG mode located at the inner layer of the five period RPC shell with inverted sequence (a-type and b-type layers have been exchanged with respect to Fig. 1). The monopolar WG0 mode with frequency 0.4575 is depicted. Note the high concentration of the field in the cavity due to the leaky nature of this mode. The insets show the E-field pattern in 2D for comparison purposes. (b) Radial dependence of the radial and angular components of the refractive index tensor.

Fig. 4(b), indicates that localization takes place in the external interface, where the last layer is of b type (with $n_r = 1$). At this point it is interesting to recall that the so called Tamm states were observed at the interface between a multilayered dielectric structure and the background.[17] The Tamm states are strongly localized at the last layers of the multilayers due to the high contrast between the refractive index of the last layers and the background. In contrast, our WGMs, these being a kind of surface states with circular symmetry, are slightly localized and, therefore, highly radiative.

It is possible to obtain WGMs localized in the inner layer of the shell by simply inverting the sequence of alternating a- and b-type layers. Figure 5(a) shows the case of a WGM with monopolar symmetry ($q = 0$) that has been obtained using an inner layer b type and an outer layer a type [this is an opposite configuration as compared to Fig. 4(b)]. The inset shows the 2D field pattern of this mode that resonates at 0.4575 (in reduced units), a value very close to that of the WG0 mode localized in the outer layer of the shell (0.4724). From Fig. 5(a), the high concentration of field observed inside the cavity (gray area) is due to leakage of the interface mode to the inner cavity. At the resonance frequency of the interface WG mode, a multiple of the free-space wavelength is close to a value commensurate with the cavity diameter ($\phi = 2r_{\text{int}}$), i.e., $\phi \approx 3\lambda/2$. Three lobes in the E-field curve appear in practice along the diameter of the inner cavity. The radial profiles of the E field shown in Figs. 4 and 5, in comparison with the corresponding radial dependencies of components n_r and n_θ, allow us to conclude that localization of these types of modes is strongly related to regions with high n_θ.

Figure 2(c) shows that the spectral peaks of WGMs localized at the inner layer are narrower than their counterparts localized at the external layer [see Fig. 2(b)]. This means that the internal WGMs present a strong localization character in comparison with the external WGMs.

It has been pointed out that the main feature of WGMs localized at the external layers of RPC shells is that they are highly radiative. In other words, they have very low Q factors, a property of paramount interest in building devices for energy harvesting. The Q factors of WGMs are specifically studied in the next section in comparison with the Q factors of cavity and FP resonances.

IV. ENERGY HARVESTING WITH WHISPERING GALLERY MODES

Energy absorption and harvesting is a topic of great interest where artificially structured materials have shown potential

advantages.[3,22–24] In this context, we consider here a specific configuration of RPC shells that enhances the energy exchange between their resonant WGMs with the background EM fields. The concept of energy harvesting is therefore considered here as the ability of a given structure of exchanging with and trapping EM energy from the surrounding medium. For this purpose, structures based on low-Q resonators are preferred in opposition to high-Q resonators that have low coupling efficiency of EM radiation to the resonator. In what follows we describe a metamaterial shell having WGMs with extremely low Q factors.

A metamaterial shell is designed here for operating at frequencies around $f = 3$ GHz (i.e., for wavelengths around $\lambda = 100$ cm). The shells under study have radial period $d = 2$ mm ($d_a = d_b = d/2$), the central cavity has radius $r_{\text{int}} = 0.5$ mm ($r_{\text{int}} = d/4$), and the constitutive parameters of the alternating layers are

$$\mu_{ra}(r) = \frac{9.6d}{r}, \quad \mu_{rb}(r) = \frac{7.2d}{r}, \tag{27}$$

$$\mu_{\theta a}(r) = \frac{24r}{d}, \quad \mu_{\theta b}(r) = \frac{12r}{d}, \tag{28}$$

$$\varepsilon_{za}(r) = \frac{8.4d}{r}, \quad \varepsilon_{zb}(r) = \frac{49d}{r}. \tag{29}$$

These parameters are selected to produce WG modes with extremely low Q factors. The profiles for these parameters together with those of the components of the refractive index tensor are described in Figs. 6(a) to 6(c). The constitutive parameters roughly vary between 1 and 80, a stronger variation than those depicted in Fig. 1.

The practical realization of artificial structures with the profiles shown in Figs. 1 and 6 is not an easy task and it involves a designing procedure that is beyond the scope of the present work. However, the reader is referred to Ref. 11 where it was demonstrated how radial photonic shells with moderates values of permittivity and permeability were designed and fabricated using concentric layers of split ring resonators (SRR). For the large values of permittivity and permeability studied here the use of SRR might not be the best approach. Instead, small inclusions (cubes or spheres) of ferroelectric materials (to obtain high permittivity) together with magnetic resonance effects in high permittivity dielectrics (Mie resonances) could be a better solution.

For the sake of comparison, the Q factors of the FP-like modes and cavity modes have also been calculated as a function of the number N of double layers. Results have been obtained using the TMM described in Sec. III and have been compared with the ones calculated using commercial software.[21] Only radiation losses are considered in all the calculations. The possible dissipative losses associated with the materials have been neglected in this first approach.

Figures 7(a) and 7(b) show the results obtained for the resonance frequencies and Q factors, respectively, of the FP-like modes. Modes with dipolar ($q = 1$), quadrupolar ($q = 2$), and hexapolar ($q = 3$) symmetries are studied. The FP-like mode for a given symmetry corresponds to the lowest frequency mode within the pass band. Note the excellent agreement between the values calculated with the TMM (dashed lines) and the commercial software COMSOL (continuous lines).

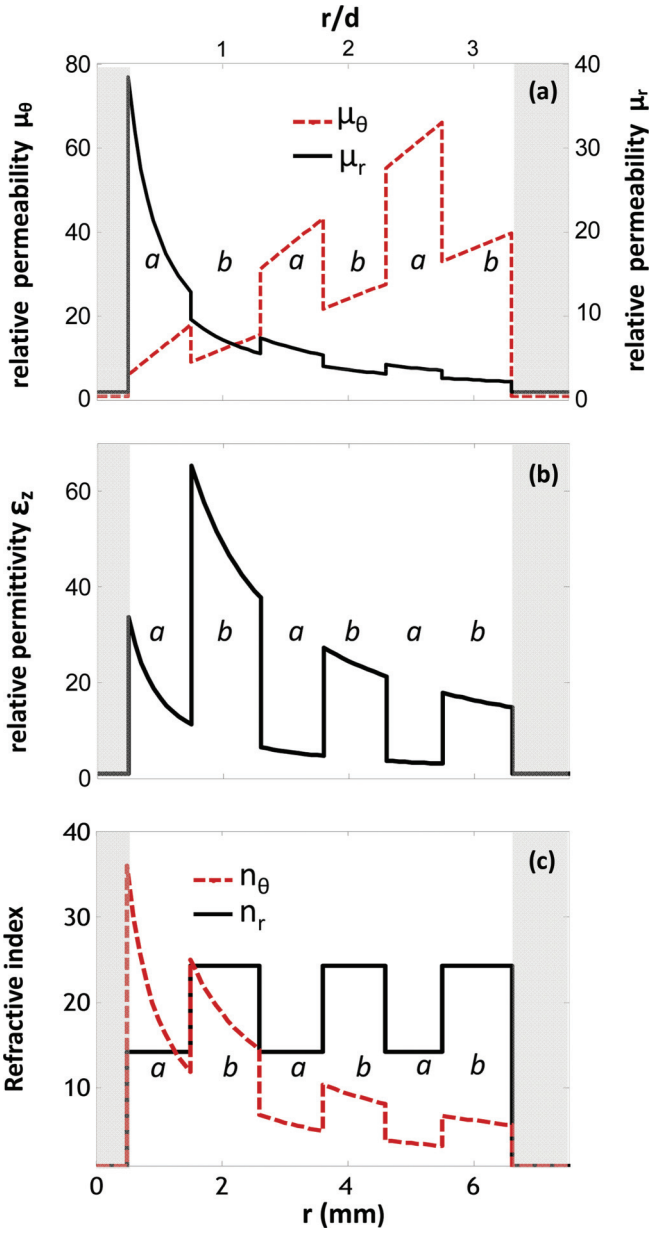

FIG. 6. (Color online) Profiles of the constitutive parameters defining an anisotropic metamaterial shell made of five periods of alternating materials and having a central cavity with radius $r_{\text{int}} = 2d$. (a) Radial and angular permeabilities μ_r and μ_θ, (b) permittivity ε_z, and (c) radial and angular components of the refractive index n_r and n_θ, respectively.

The main features of these modes are the slight frequency variation as a function of the number of layers (upper panel) and also the small variation of the Q factor (less than one order of magnitude).

Figure 8 shows the results corresponding to the cavity modes. Figure 8(a) shows that their frequencies remain constant as a function of the number of layers N and are very high in comparison with that of FP modes. High frequency values are explained because of the small dimensions of the cavity. For this type of mode, only TMM calculations are reported since the commercial software, which is based on the finite elements method, is not efficient in simulating large electrical

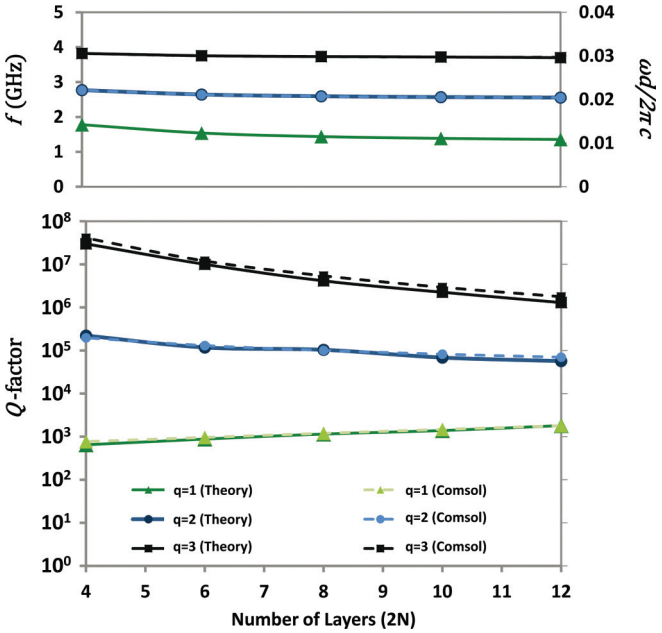

FIG. 7. (Color online) Frequency variation (a) and quality factor Q variation (b) as a function of the number N of periods for the Fabry-Perot resonances located in the shell described in Fig. 6. The radius of the cavity being $r_{\text{int}} = 0.5$ mm. Results from a commercial software (COMSOL) are compared with the transfer matrix method (TMM).

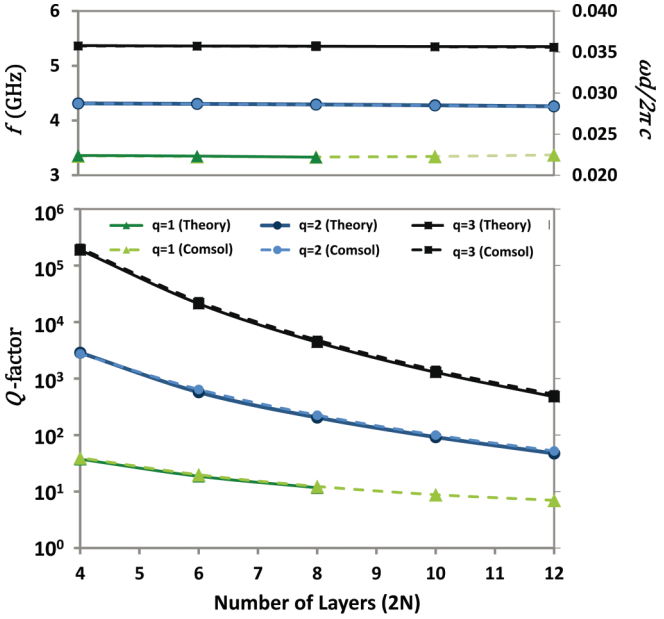

FIG. 9. (Color online) Frequency variation (a) and quality factor Q variation (b) as a function of the number N of periods for the outer interface whispering gallery resonances located in the shell described in Fig. 6. The radius of the cavity being $r_{\text{int}} = 0.5$ mm. Results from a commercial software (COMSOL) are compared with the transfer matrix method (TMM).

size objects. Figure 8(b) shows that the corresponding Q factors exponentially increase with N. This can be understood as a consequence of the exponential decaying behavior of the E field within the photonic band gap. A similar behavior was

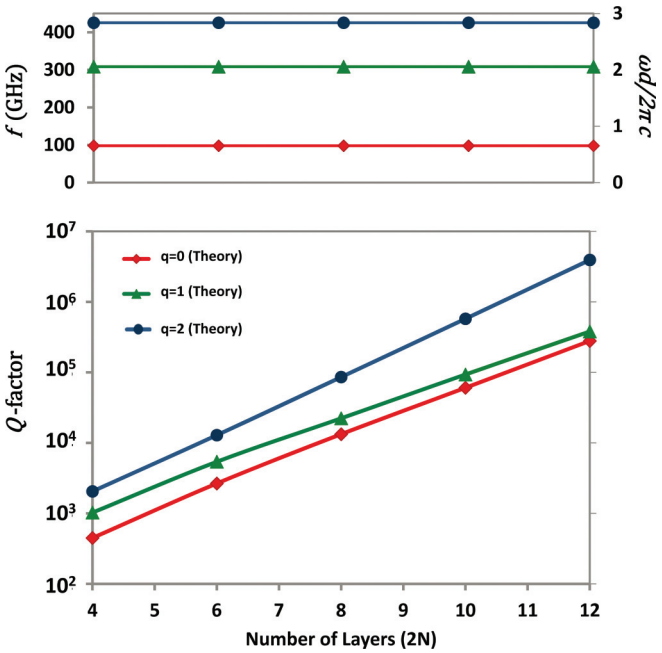

FIG. 8. (Color online) Frequency variation (a) and quality factor Q variation (b) as a function of the number N of periods for the modes located in the inner void cavity of the shell described in Fig. 6. The radius of the cavity being $r_{\text{int}} = 0.5$ mm. Results are obtained with the transfer matrix method (TMM).

observed for the cavity modes confined in RACs. The reader is referred to a previous work[20] for a detailed discussion of the properties of cavity modes in anisotropic and inhomogeneous acoustic shells.

Let us point out that the behavior of FP-like modes and cavity modes is completely analogous to the corresponding modes studied in the acoustic counterparts of these photonic structures, the metamaterial shells based on RAC.[20] The energy harvesting carried out by EM or acoustic waves would be more efficient with resonant modes with the lowest Q factors. Then, with this goal in mind, cavity modes in a metamaterial shell made of a small number of layers are preferable. However, WGMs can be obtained with lower Q factors as it is explained below.

Figure 9 reports the properties of WGMs localized at the outer shell surface as a function of N. Figure 9(a) shows that their frequencies have a negligible dependence with the shell thickness. Their values for $N = 2$ (four layers) are 3.35 GHz (WG1), 4.29 GHz (WG2), and 5.36 GHz (WG3). For the case $N = 1$ (a double layer) no surface mode was obtained since the band gap concept cannot apply to a single period shell. Again, results obtained with our analytical TMM are well supported by the numerical experiments using COMSOL.

A very remarkable property of these modes is that their frequencies, as in the case of cavity modes, do not vary with the shell thickness. This would seem counterintuitive since the frequency of WGMs in cylindrical cavities made of isotropic dielectric medium depends on the optical path determined by the cavity perimeter; that is $\ell = n \times 2\pi R$, where n is the refractive index and R is the cavity radius. For the anisotropic and inhomogeneous shell under consideration, Fig. 6(c) shows that n_r is constant within each layer of types a or b, their

values alternate in consecutive layers between $n_{ra} = 15$ and $n_{rb} = 25$. Since the external layer (of b type) has a higher angular refractive index n_θ, compared to the background or the closest shell layer (of a type) it may guide some energy in the angular direction. Conditions exist for these modes to be propagative within the external b layer, and this time again resonant modes appear due to the finite size of the perimeter of this external layer. The refractive index in this perimeter varies as $n_\theta = \sqrt{\varepsilon_z \mu_r} \propto 1/r$, which is an inverse function of the radial distance [see Eqs. (27) to (29)]. Now, this refractive index with inverse radial dependence makes that the "optical path" ($\sim n_\theta \times 2\pi r = ct$, with ct being a constant) of the outer layer is independent of the size (or number of layers) of the shell. This explains the constant resonant frequencies of the whispering gallery modes and their independence with respect to the number of layers.

Figure 9(b) indicates that the Q factors decrease with the thickness of the shell, an interesting feature that can be useful for energy harvesting. We may provide an intuitive explanation for this observed feature. The decreasing values of Q when the size of the shell increases are related to the occurrence of WGMs in the band gaps of the multilayer shell. It is clear that in the respective band gap propagation of the EM wave of the WG mode in the radial direction and towards the center of the structure is prohibited (WGMs only "travel" in the angular direction). This is one of the requirements for the existence of these modes. When we consider finite size shells, thicker multilayers that produce the exponential tails of the E field towards the center will not reach the inner cavity and lose localization in comparison with thinner shells. It is observed in Fig. 9 how the Q factors converge to an apparently common value for an increasing number of layers. This common value is necessarily the one corresponding to the surface mode weakly localized at the interface between the background with the semi-infinite structure. Note that mode WG1 has the lowest Q factor among all the modes analyzed here. For the higher order WGMs, their Q factors are 2 orders of magnitude lower than those calculated for the FP-like modes with similar order. In comparison with the Q factors obtained for cavity modes C1 and C2, WG1 has a Q-factor comparable with that of C1 at $N = 2$, while WG2 has a Q factor 2 orders of magnitude larger (at $N = 2$). However, for increasing shell thickness WGMs strongly decrease their Q factor up to values several orders of magnitude lower than that of the cavity modes. It can be concluded that WGMs associated with a thick enough metamaterial shell are the best candidates to guarantee an efficient energy exchange with the EM waves to/from the background.

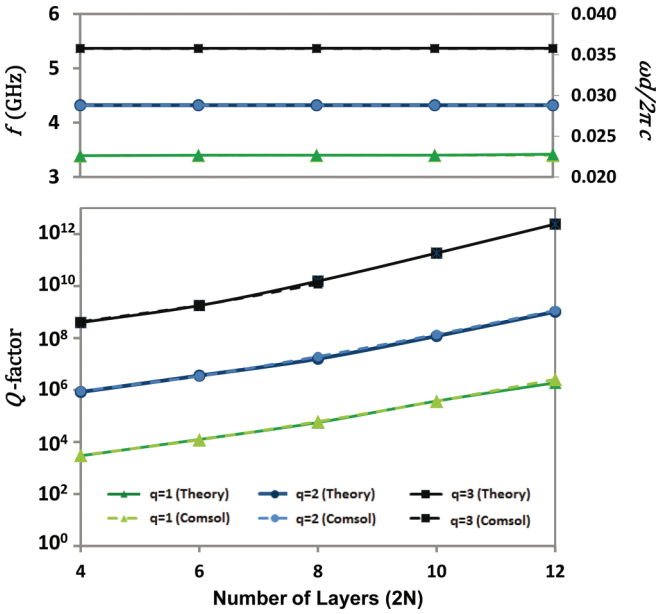

FIG. 10. (Color online) Frequency variation (a) and quality factor Q variation (b) as a function of the number N of periods for the inner interface whispering gallery resonances located in the shell described in Fig. 6 when the layer order of a and b types is inverted. The radius of the cavity being $r_{\text{int}} = 0.5$ mm. Results from a commercial software (COMSOL) are compared with the transfer matrix method (TMM).

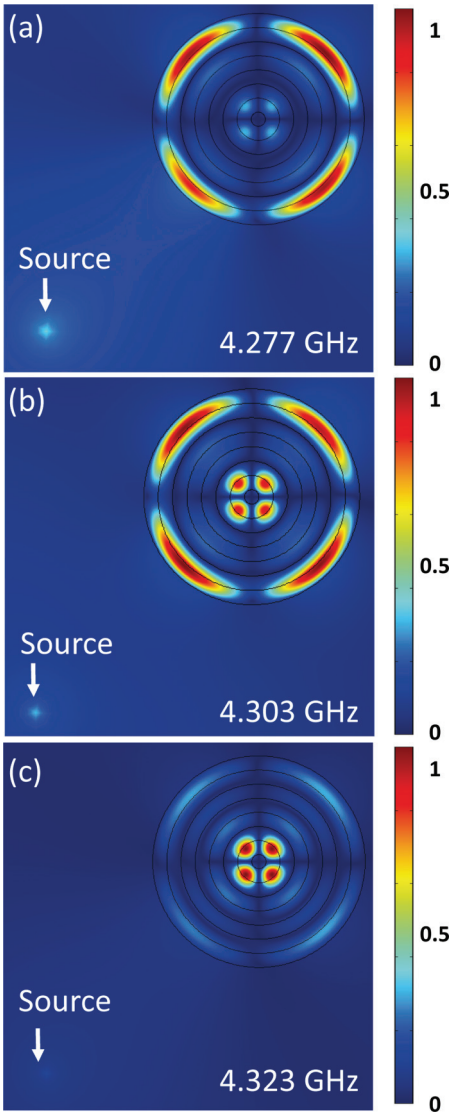

FIG. 11. (Color online) E-field patterns of an external point source illuminating a RPC shell and exciting a whispering gallery mode, (a) an external whispering gallery mode at 4.277 GHz, (b) simultaneous excitation of internal and external whispering gallery modes at 4.303 GHz, and (c) internal whispering gallery mode at 4.323 GHz. Here the total number of layers of the shell is seven, with inner and outer layers of the same a type.

If the layer order is inverted (i.e., higher n_θ value for the inner interface layer), the previously observed WGMs are transferred to that interface. The behavior of these modes is described in Fig. 10 and is coherent with the previous discussion. Again, the resonant frequencies of the WGM of the inner interface are independent of the size of the shell. This behavior is obvious for this configuration since the circular dimension of the inner layer is kept constant when adding external layers. Resonant frequencies are only slightly shifted with respect to those of Fig. 9. In coherence also with the previous discussion, the Q factors obtained increase with the number of layers since the exponential tail is smaller at a larger distance from the inner surface. In other words, the internal WGMs will be increasingly isolated with respect to external background and, therefore, the radiation losses will be smaller (i.e., higher Q factors). However, the Q-factor variation with the number of layers is not exponential as it was in the case of cavity modes (see Fig. 8).

Finally, let us discuss the case of two degenerate WGMs obtained for a single shell, one being located at the outer boundary and the other at the inner boundary. This case is achieved considering a shell with an odd number of layers (seven layers equivalent to three periods and one additional b-type layer); the total diameter being equal to $\phi = 15$ mm. Figure 11 reports how a point source located at a distance $r_{\text{source}} = 20$ mm ($\equiv 10d$) from the shell center illuminates the shell for three slightly different frequencies. It is shown how the WG2 mode at the outer layer is excited at 4.277 GHz, while the WG2 mode at the inner layer is excited at 4.323 GHz. Moreover, Fig. 11(b) shows that both modes are simultaneously excited at 4.303 GHz. The frequency differences are much smaller than those depicted in Figs. 4 and 5 since the inner void cavity size is much (electrically) smaller and there is a lower perturbation due to it. In the case depicted in Fig. 11(c), the resonant mode is linked to the inner interface of the shell with the cavity. In order to complete this graphical information, the Q factors of these two degenerate modes have been calculated showing a non-negligible difference. For the external WGM shown in Fig. 11(a) we obtained the value $Q_{\text{WG2\_ext}} = 503$, whereas for the internal WGM shown in Fig. 11(c) $Q_{\text{WG2\_int}} = 1824$. This difference is expected since the internal WGM is more isolated from the external background and, consequently, is less radiative.

This is a representative example of how the WGMs can be used as a mechanism for improving the energy harvesting from external EM waves and collecting it at the central active area. Although it is not the purpose of this paper to design a practical device that optimally gathers energy radiated in its surroundings, one can note from Fig. 11 that electric field (and hence energy) tends to concentrate in the interface layers rather than close to the source position. We understand this fact is a proof of the ability of the device to harvest EM energy.

In spite of the rigorous results previously discussed, a word of caution should be added regarding the possible effects that losses will play in the artificial structures with the required radially dependent constitutive parameters (permittivity and permeability). It has been pointed out that these structures will be based on arrays of individual units with local resonances. Therefore, the losses associated with resonance effects will degrade the performance of the anisotropic shells based on them. The performance will be deteriorated up to a quantity that will depend of our ability to select the best (low loss) materials and the designing procedure. Since our target here is to produce WGM with low Q, the intrinsic losses should not be a severe drawback and the radiation losses, which do consider here, will be the dominant loss contribution.

V. CONCLUSION

We have analyzed the existence of low-Q whispering gallery modes at the interface layers of anisotropic and inhomogeneous metamaterial shells. Conditions for these modes to exist are basically the existence of prohibited band gaps in the dispersion diagram of the shell and interface layers with high refractive index as compared to the background. These modes present the particular feature of having resonant frequencies independent of the shell thickness, a property allowing adapting the quality factor of the resonant modes in a very simple manner. At the same time, energy exchanges with electromagnetic waves in the surrounding background are favored, allowing the use of the anisotropic metamaterial shells as a means of harvesting electromagnetic energy. Particularly, broadband operation by the reported low-Q whispering gallery modes can be obtained by changing the properties of the cavity medium, like its radius and dielectric constant.

ACKNOWLEDGMENTS

The authors acknowledge the financial support of Spanish Ministry MINECO (Grants No. TEC 2010-19751 and No. Consolider CSD2008-00066), and the US Office of Naval Research (USA). J. Sánchez-Dehesa acknowledges useful discussions with Federico Sabina and Matthew Guild.

*Corresponding author: jsdehesa@upv.es

[1]C. R. Williams, S. R. Andrews, S. A. Maier, A. I. Fernandez-Dominguez, L. Martin-Moreno, and F. J. Garcia-Vidal, Nat. Photon. **2**, 175 (2008).

[2]C. M. Watts, X. Liu, and W. J. Padilla, Adv. Mater. **24**, OP98 (2012).

[3]P. Spinelli, M. A. Verschuuren, and A. Polman, Nat. Commun. **3**, 692 (2012).

[4]B. A. Munk, *Frequency Selective Surfaces: Theory and Design* (John Wiley and Sons, Hoboken, NJ, 2000), p. 410.

[5]J. Carbonell, E. Lheurette, and D. Lippens, Prog. Electromagn. Res. **112**, 215 (2011), http://www.jpier.org/PIER/pier.php?paper=10121402.

[6]S. Wang, F. Garet, K. Blary, C. Croenne, E. Lheurette, J. Coutaz, and D. Lippens, J. Appl. Phys. **107**, 074510 (2010).

[7]M. Aznabet, M. Navarro-Cia, S. A. Kuznetsov, A. V. Gelfand, N. I. Fedorinina, Y. G. Goncharov, M. Beruete, O. El Mrabet, and M. Sorolla, Opt. Express **16**, 18312 (2008).

[8]W. Barnes, A. Dereux, and T. Ebbesen, Nature (London) **424**, 824 (2003).

[9] J. Pendry, L. Martin-Moreno, and F. Garcia-Vidal, Science **305**, 847 (2004).
[10] D. Torrent and J. Sanchez-Dehesa, Phys. Rev. Lett. **103**, 064301 (2009).
[11] J. Carbonell, A. Diaz-Rubio, D. Torrent, F. Cervera, M. A. Kirleis, A. Piqué, and J. Sánchez-Dehesa, Sci. Rep. **2**, 558 (2012).
[12] N. Horiuchi, Y. Segawa, T. Nozokido, K. Mizuno, and H. Miyazaki, Opt. Lett. **30**, 973 (2005).
[13] P. Lee, T. Lu, J. Fan, and F. Tsai, Appl. Phys. Lett. **90**, 151125 (2007).
[14] J. Carbonell, D. Torrent, and J. Sánchez-Dehesa, IEEE Trans. Antennas Propag. **61**, 755 (2013).
[15] R. F. Harrington, *Time-Harmonic Electromagnetic Fields* (IEEE–Wiley Interscience, New York, 1961).
[16] A. P. Vinogradov, A. V. Dorofeenko, S. G. Erokhin, M. Inoue, A. A. Lisyansky, A. M. Merzlikin, and A. B. Granovsky, Phys. Rev. B **74**, 045128 (2006).
[17] T. Goto, A. V. Baryshev, M. Inoue, A. V. Dorofeenko, A. M. Merzlikin, A. P. Vinogradov, A. A. Lisyansky, and A. B. Granovsky, Phys. Rev. B **79**, 125103 (2009).
[18] J. Carbonell, D. Torrent, A. Diaz-Rubio, and J. Sanchez-Dehesa, New J. Phys. **13**, 103034 (2011).
[19] A. Yariv and P. Yeh, *Optical Waves in Crystals* (Wiley, New York, 1984), p. 5.
[20] D. Torrent and J. Sanchez-Dehesa, New J. Phys. **12**, 073034 (2010).
[21] Comsol AB (Sweden), Comsol Multiphysics (v. 4.2a), www.comsol.com, 2011.
[22] Y. Yao, J. Yao, V. K. Narasimhan, Z. Ruan, C. Xie, S. Fan, and Y. Cui, Nat. Commun. **3**, 664 (2012).
[23] C. Navau, J. Prat-Camps, and A. Sanchez, Phys. Rev. Lett. **109**, 263903 (2012).
[24] J. Carbonell, F. Cervera, J. Sanchez-Dehesa, J. Arriaga, L. Gumen, and A. Krokhin, Appl. Phys. Lett. **97**, 231122 (2010).